View Article Online
View Journal

Materials
Advances

Accepted Manuscript

This article can be cited before page numbers have been issued, to do this please use: S. KHAN, K. Padmasri, U. Mondal and C. Chakraborty, *Mater. Adv.*, 2026, DOI: 10.1039/D6MA00515B.

ROYAL SOCIETY
OF CHEMISTRY

rsc.li/materials-advances

View Article Online
DOI: 10.1039/D6MA00515B

In-situ grown Synergistic Co-based metal-organic framework/graphene oxide composite for enhanced supercapacitor performance

Soumen Khan,*[a, b] K. Padmasri,[c] Unmesha Mondal,[a] and Chanchal Chakraborty*,[a,b]

[a] Department of Chemistry, Birla Institute of Technology & Science (BITS) Pilani, Hyderabad Campus, Jawaharnagar, Samirpet, Hyderabad, Telangana 500078, India.

E-mail: chanchal@hyderabad.bits-pilani.ac.in (Dr. Chanchal Chakraborty)

Email: p20220015@hyderabad.bits-pilani.ac.in (Soumen Khan)

[b] Materials Center for Sustainable Energy & Environment (McSEE), Birla Institute of Technology & Science (BITS) Pilani, Hyderabad Campus. Jawaharnagar, Samirpet, Hyderabad, Telangana 500078, India.

[c] Department of Chemical Engineering, Birla Institute of Technology and Science-Pilani, Hyderabad Campus, Jawaharnagar, Samirpet, Hyderabad, Telangana 500078, India.

Keywords: Co-based metal-organic framework; graphene oxide; *in-situ* composites; supercapacitors; specific capacitance.

Abstract

The use of pristine metal-organic frameworks (MOFs) as active electrodes for energy storage is challenging in practice due to their low conductivity and electrochemical durability. To increase the energy storage performance of the pristine MOF, an *in-situ* graphene oxide (GO) composite of a cobalt succinate MOF (abbreviated as Co-MOF) is designed using cheap, commercially available starting materials for an energy storage electrode. Herein, we demonstrate the MOF-GO composite with GO weight percentages of 5% (Co-MOF-GO5) and 10% (Co-MOF-GO10) to elucidate the potential of these composites for high-performance supercapacitors. Among all, the Co-MOF-GO5 exhibits the highest specific capacitance of 552 F/g, with upright cycle stability of 5000 and better energy density (33 Wh/kg) and power density (2.9 kW/kg) in a three-electrode cell system compared with pristine Co-MOF and other composites. The calculated electrochemically active surface area (ECSA) and lower charge transfer resistance also support the better performance of the Co-MOF-GO5 compared to Co-MOF-GO10. To assess the practical applicability of Co-MOF-GO5 as an energy storage material, symmetric CR2032 coin-cell devices were fabricated by using the Co-MOF-GO5 at

View Article Online
DOI: 10.1039/D6MA00515B

both electrodes with aqueous KOH electrolyte, which can power a commercially available light-emitting diode bulb (~1.8 V) for a few minutes.

1. Introduction:

Rapid exhaustion of fossil fuels, amid rising environmental and geopolitical concerns, has increased demand for sustainable and effective energy storage solutions.[1-3] Renewable sources like wind and solar are promising alternatives, but their intermittent nature creates challenges for grid reliability. As a result, advanced energy storage systems capable of delivering high power and long-term durability are much required to overcome the recent energy crisis.[4,5] Amongst the accessible technologies, like supercapacitors (SCs), conventional capacitors, batteries, and fuel cells, SCs have appeared as striking candidates owing to rapid charge-discharge ability, high power and energy density, long-term cyclability, and the safety in operation.[6-10] However, their comparatively low energy density compared to batteries remains a main limitation, which can be resolved by judicious design of the electrode materials for SCs.[11-13]

Active electrode materials carry a pivotal role in determining the electrochemical performance of SCs. To date, a variety of materials, including carbon materials, transition-metal-based oxides or hydroxides, and conducting polymers, have been widely studied in this regard.[14,15] Carbon-based materials offer excellent electrical conductivity and cycling durability, but they typically store charge only through electric double-layer capacitance (EDLC), which results in a limited energy density.[16,17] On the other hand, redox-active metal oxides or conducting polymers exhibit high capacitance via faradaic redox reactions, known as pseudocapacitance, which provides better energy density, but these systems may often suffer from poor cyclability and low rate capability.[18,19] Therefore, rational design of the hybrid electrode materials, which can integrate the EDLC as well as pseudocapacitive contributions, has developed a widely adopted approach for overcoming these intrinsic limitations.[20-24]

From this perspective, metal-organic frameworks (MOFs) have recently attracted substantial attention as next-generation electrode materials for sustainable energy storage and conversion systems.[25-30] MOFs are porous crystalline materials with high surface areas in which metal ions or clusters are coordinated to organic ligands, offering structural tunability to manipulate surface areas, pore sizes, and the abundance of redox-active metal centers.[31-34] All these unique structural features make the MOFs fascinating candidates for SC-based energy

View Article Online
DOI: 10.1039/D6MA00515B

storage electrodes, combining high surface-area EDLC and redox-based pseudocapacitive charge storage via the reversible redox reactions at the metal/ligand centers.[35-38] Nevertheless, the practical application of pristine MOFs in sustainable supercapacitors is severely hindered by their low intrinsic electrical conductivity and moderate structural stability across different electrochemical conditions during redox process.[39,40] Keeping all of these in perspective, noteworthy efforts have been made to develop MOF-based composites by integrating the carbon-based materials such as graphene oxide (GO), carbon nanotubes, reduced graphene oxide, metal nanoparticles or conducting polymers.[39,41-44] Among all of these, GO stands out for its larger specific surface area, oxygen-containing functional groups, exceptional mechanical flexibility, and strong interfacial interactions with MOF frameworks.[39-40] Not only does GO enhance the charge transfer process, but it also suppresses particle accumulation, facilitating better ion diffusion and improving electrode/electrolyte wettability.[41-44] Remarkably, the growth of MOFs on GO sheets is well-designed beyond the physical mixing process, as it allows close interfacial contact, structural reliability, and long-term electrochemical durability by avoiding component exclusion during charging-discharging cycles.

Cobalt-based MOFs are attracting particular attention for SC applications owing to the rich redox chemistry of the Co^{2+}/Co^{3+} couple, which can provide high pseudocapacitive contributions.[45-48] Though reports on cost-effective, environmentally friendly cobalt-carboxylate MOFs with carbon-based materials like GO are available in the literature, their rational integration with graphene oxide via an *in-situ* synthesis process to provide better interfacial contact remains in demand. In addition, systematic research correlating GO content with electrochemical performance is crucial to identify optimal compositions that balance conductivity enhancement with ion-accessible active metal sites.[39] Herein, we report a one-pot nimble *in-situ* synthesis approach of GO-integrated Co-MOF (Co-MOF-GO) composites using cheap and commercially accessible precursors. By carefully tuning the GO content (5 and 10 wt%), we reveal that the optimized Co-MOF-GO5 composite exhibits better electrochemical performance than pristine Co-MOF and other composite counterparts. The synergistic interface between the redox-active Co-MOF and GO sheets results in improved charge transport, faster ion diffusion, higher electrochemically active surface area (ECSA), reduced internal resistance, and superior cycling durability.[39] Additionally, the practical application possibility of the improved electrode is authenticated through the fabrication of a symmetric CR2032 coin-cell SC capable of powering a commercial LED. This work provides valuable insights into the *in*

View Article Online
DOI: 10.1039/D5MA00515B

situ composite formation of MOF/GO to enhance energy storage performance through synergistic interfacial coupling, enabling cost-effective supercapacitor systems.

The actual uniqueness of the work lies in the selection of a non-aromatic, simple aliphatic dicarboxylate linker (succinate), inexpensive, commercially accessible precursors, and a water-mediated synthesis route, which result in lower synthetic complexity, better scalability, lower cost, and a greener synthesis pathway. The *in-situ* growth strategy enables intimate heterointerfacial contact between the cobalt succinate framework and GO nanosheets, unlike conventional physically mixed composites. The enhanced performance arises from the cooperative coupling of diffusion-controlled pseudocapacitance from Co-redox centres, the surface EDLC contribution from GO, and interfacial charge-transfer synergy, which influence one another's structural and electrochemical stabilisation.

2. Experimental section

2.1. Materials

All chemicals and reagents were obtained from commercial vendors and applied exactly as supplied. Sigma-Aldrich and Sisco Research Laboratories (SRL) Pvt. Ltd. in India provided cobalt chloride hexahydrate ($CoCl_2 \cdot 6H_2O$), succinic acid, potassium hydroxide (KOH), Nafion, carbon black, ethanol, methanol, sulphuric acid (H_2SO_4), graphite powder, sodium nitrite ($NaNO_2$), potassium permanganate ($KMnO_4$), hydrogen peroxide (H_2O_2), potassium iodide (KI), ammonia, and other solvents. The deionized water was used to prepare the KOH electrolyte solution for electrochemical analysis. GRS Corporation, India, delivers nickel foam (width ≤ 1000 mm, thickness ≤ 2.5 mm). GO was synthesized as described in our previous report. [48]

2.2. Synthesis of Co-MOF

Co-MOF was synthesized using the previous protocol.[48-51] In a 100 mL beaker, 4 g (33.87 mmol) of succinic acid and 3.8 g (67.74 mmol) of KOH were taken. To this, about 15 mL of water was added, followed by sonication for 15 minutes to dissolve the material to get a clear solution (solution A). The solution was then transferred to a 100 mL round-bottom (RB) flask. In another beaker, 8.33 g (35 mmol) of cobalt chloride ($CoCl_2 \cdot 6H_2O$) and 10 mL of water were added, followed by sonication for 15 min to obtain a clear solution, designated as solution B. Then, solution B was added dropwise to solution A with continuous stirring. After complete addition, the solution was refluxed at 110 ºC for 24 hours to provide crystalline Co-MOF with 90% yield.

2.3. Synthesis of Co-MOF/GO composites

For the synthesis of Co-MOF-GO5, first, 416 mg GO (5 wt% with respect to the metal salt) was dispersed in 100 mL of distilled water and sonicated for 3 h. Then, the GO dispersion was kept standing for 1 h, and sonicated for another hour. Finally, in the GO solution, 4 g (33.87 mmol) of succinic acid and 3.8 g (67.74 mmol) of KOH were taken. To this, about 15 mL of water was added, followed by sonication for 15 minutes to get a clear solution (solution A). The solution was then transferred to a 100 mL RB flask. In another beaker, 8.33 g (35 mmol) $CoCl_2 \cdot 6H_2O$ and 10 mL of water were added, followed by sonication for 15 min to obtain a clear solution, designated as solution B. Then, solution B was added dropwise to solution A with continuous stirring. After complete addition of solution B to solution A, the mixture was refluxed at 110 ºC for 24 hours to yield the Co-MOF-GO5 composite. The 10 wt% GO composite (with respect to the metal salt), Co-MOF-GO10, was synthesized using a similar protocol.

2.4. General Physicochemical Characterization Tools

The FTIR spectra of Co-MOF and Co-MOF-GO composites were recorded in ATR mode in the range of 4000-500 cm^{-1} using a Bruker-Alpha-II-Platinum ATR. UV-vis spectroscopic studies were carried out using a JASCO V-670 spectrometer. PXRD data were recorded on a Rigaku Ultima IV X-ray diffractometer for all the samples under constant parameters. Field-emission scanning electron microscopy (FESEM) and energy-dispersive X-ray analysis (EDX) of the drop-cast samples on a silicon wafer were performed with a FEI ApreoS FESEM instrument at 20 kV. The thermal stability of the samples was analyzed using a Shimadzu DTG-60 TGA instrument over the temperature range of 30 to 800 °C at a heating rate of 10 °C min-1 under a N_2 atmosphere.

2.5. Electrochemical Measurements:

The pretreated Ni-foams were used for the electrochemical analysis of Co-MOF and its composites. The 10 mg Co-MOF or its composites were dispersed in 1 mL of DMF and mixed with 10 μL of Nafion and 1 mg of carbon black to form a slurry, which was then cast onto a Ni-foam (1×1 cm) electrode and dried in a vacuum oven at 60 ℃ for the study. The mass loading of Co-MOF is 0.5 mg/cm^2.

View Article Online
DOI: 10.1039/D5MA00515B

Electrochemical analyses, such as cyclic voltammetry (CV), galvanostatic charge-discharge (GCD), and electrochemical impedance spectroscopy (EIS) of the synthesized electrode materials, were performed in a three-electrode system using the OrigaFlex OGF500 electrochemical workstation. 1 M KOH was used as the electrolyte for all experiments, Ag/AgCl as the reference electrode, and a Pt wire as the counter electrode. Ni foam was used as a current collector here. Electrochemical impedance spectroscopy (EIS) was performed over the frequency range of 1 Hz to 1 kHz using an AC perturbation.

2.5 Determination of the energy storage parameters

The gravimetric capacitance (C_g) determined from the constant current discharge curves was calculated using the following equations: [20,37,48,50,51]

$$\boldsymbol{C_g = \frac{I \times \Delta t}{m \times \Delta V}} \text{ (F g}^{-1}\text{)} \text{ ………………… } \mathbf{(1)}$$

Where, C_g (F g^{-1}) is gravimetric capacitance, Δt is discharge time (s) determined from GCD study, ΔV is the potential window (V), I is the constant current used for charging and discharging (mA), and m active mass of the material on one Ni-foam electrode exposed in the electrolyte (mg). The gravimetric energy density (ED) and power density (PD) are calculated according to the following two equations:

$$\mathbf{ED}\left(\mathbf{\frac{Wh}{kg}}\right) = \boldsymbol{\frac{C_g \times \Delta V^2}{2 \times 3.6}} \; (Wh\;kg^{-1}) \text{………………… } \mathbf{(2)}$$

$$\mathbf{PD}\left(\mathbf{\frac{W}{kg}}\right) = \frac{\mathrm{ED}}{\Delta t} \times 3600 \; (W\;kg^{-1}) \text{………………… } \mathbf{(3)}$$

The coulombic efficiency (η) was evaluated from the following equation:

$$\boldsymbol{\eta = \frac{t_d}{t_c} \times 100\%} \text{ .... } \mathbf{(4)}$$

Where t_d is the discharging time, and t_c is the charging time. The following equation calculated the equivalent series resistance (ESR):

$$\mathbf{ESR} = \boldsymbol{\frac{V_{drop}}{2I}} \text{ …………………} \mathbf{(5)}$$

Here, $\boldsymbol{V_{drop}}$ is the voltage drop at the beginning of the discharge curve, and $\boldsymbol{I}$ is the discharge current. To investigate the real-world applicability of the synthesized Co-MOF-GO composite electrode material for energy storage, a symmetric CR2032 coin-cell-based supercapacitor configuration was developed, with similar mass loadings of active materials on Ni-foam current collectors on both sides.

View Article Online
DOI: 10.1039/D6MA00515B

3. Results and discussion

The crystal structure of cobalt succinate tetrahydrate, $[Co(H_2O)_4(suc)]$, is well known and structurally similar to those of its complement MOFs with Ni, Fe, Mg, and Mn.[48, 49] In contrast to earlier reports that relied on slow solvent evaporation, a straightforward, environmentally friendly synthetic method has been employed here to prepare the Co-based MOF. The structural investigation reveals that the Co(II) center adopts an octahedral coordination environment, coordinated by two oxygen atoms from succinate ligands and four water molecules.[48, 49] The succinate ligands hold the axial positions, whereas the water molecules are arranged in the equatorial plane (**Fig. 1a**). Each succinate-coordinated cobalt (II) centre can be labelled by an empirical coordination environment of AB_2M_4. The succinate ligand binds through its two carboxylate groups in a monodentate manner, each coordinating to cobalt centres and extending the structure into a one-dimensional chain. Furthermore, the strong hydrogen bond between the coordinated water molecules and the carboxylate groups links adjacent chains, causing slight geometric distortion and contributing to the overall structural durability.

To enhance the EDLC contribution, graphene oxide is incorporated in the MOF through synthesis (**Fig. 1b**).[39] GO was synthesized from graphite powder according to our previous report.[48] By changing the GO wt% (5%, 10% with respect to metal wt%), two different *in-situ* MOF-GO composites were synthesized using the hydrothermal process, abbreviated as Co-MOF-GO5 and Co-MOF-GO10 (**Fig. 1c**). It is noteworthy that the *in-situ* grown nanocomposites are superior compared to physical mixing, as it can provide improved integrated systems with better interfacial coupling in homogeneous composite.[39]

View Article Online
DOI: 10.1039/D6MA00515B

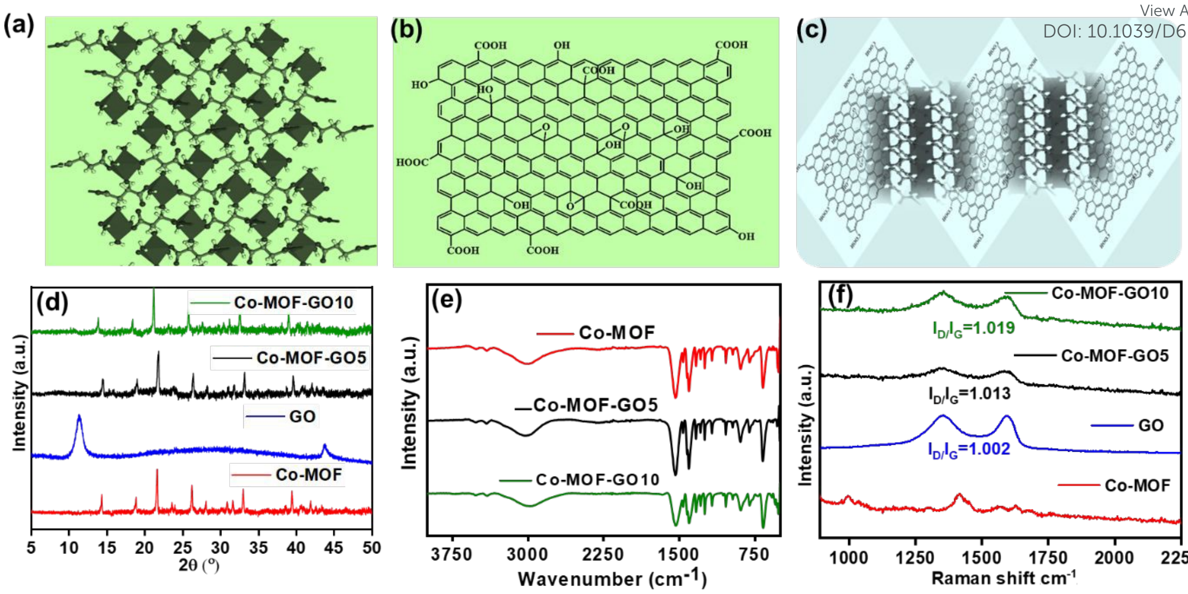

Fig. 1. (a) Packing diagrams of Co-MOF; (b) Layer of GO; (c) Plausible interaction image of the Co-MOF-GO composites; (d) PXRD patterns of the as-synthesized Co-MOF one with GO and various wt.% GO composites; (e) FT-IR spectra of Co-MOF, Co-MOF-GO5 and Co-MOF-GO10; (f) Raman spectra of Co-MOF, GO, Co-MOF-GO5, and Co-MOF-GO10.

The phase transparency of the synthesized Co-MOF and its GO composites was assessed using a PXRD study (Fig. 1d). The Co-MOF diffraction pattern was collected over the 2θ range of 5-45°, showing excellent agreement in peak locations with the referenced PXRD pattern of the compound, confirming the effective construction and high phase purity of the Co-MOF.[48-51] The functional groups present in the Co-MOF and its composites have been confirmed by FTIR analysis, as shown in Fig. 1e. A broad peak observed at 3500-3000 corresponds to the presence of water molecules in Co-MOF. The small, narrow peak for ν(O−H) at 3521 is attributed to strong hydrogen bonds. The peaks at 1532, 1456, 1403,1330, and 1243 cm^{-1} appear owing to carboxylate ions, O-H bending, and C-O, confirming the coordination with the organic ligand. The ν as(C–C) stretching was observed at 1174 cm^{-1}.[48] Raman spectra of Co-MOF, GO, and their composites are shown in Fig. 1f, which clearly reveal two distinct peaks at 1351 and 1595 cm^{-1}, corresponding to the typical D (defect and disorder) and G (graphitic) bands of the samples. Raman spectrum intensity ratios of these bands (I_D/I_G) generally indicate the degree of structural disorder and the intensity of defects. The I_D/I_G ratios were determined to be 1.013 and 1.019 for Co-MOF-GO5 and Co-MOF-GO10, respectively. The I_D/I_G values specify the presence of more defect sites (sp^3) in the Co-MOF-GO10 structure than in Co-MOF-GO5. The Raman analysis indicates higher graphitic ordering, greater electrical conductivity, and easier electron transfer in Co-MOF-GO5 than in Co-MOF-GO10,

View Article Online
DOI: 10.1039/D6MA00515B

suggesting a higher energy storage capacity can be achieved in Co-MOF-GO5. The features below 1000 cm^{-1} in the Raman Spectra of Co-MOF reveal the vibrations for Co-O coordination at ~480 cm^{-1}, Co-O coupled mode with O-C-O at 640 cm^{-1}, coupled C–C/C–O vibrational mode of coordinated succinate ligand influenced by Co–O bonding at 875 cm^{-1}, and C-C stretching at ~1000 cm^{-1}, as shown in Fig. S1in the Electronic Supplementary Information (ESI).

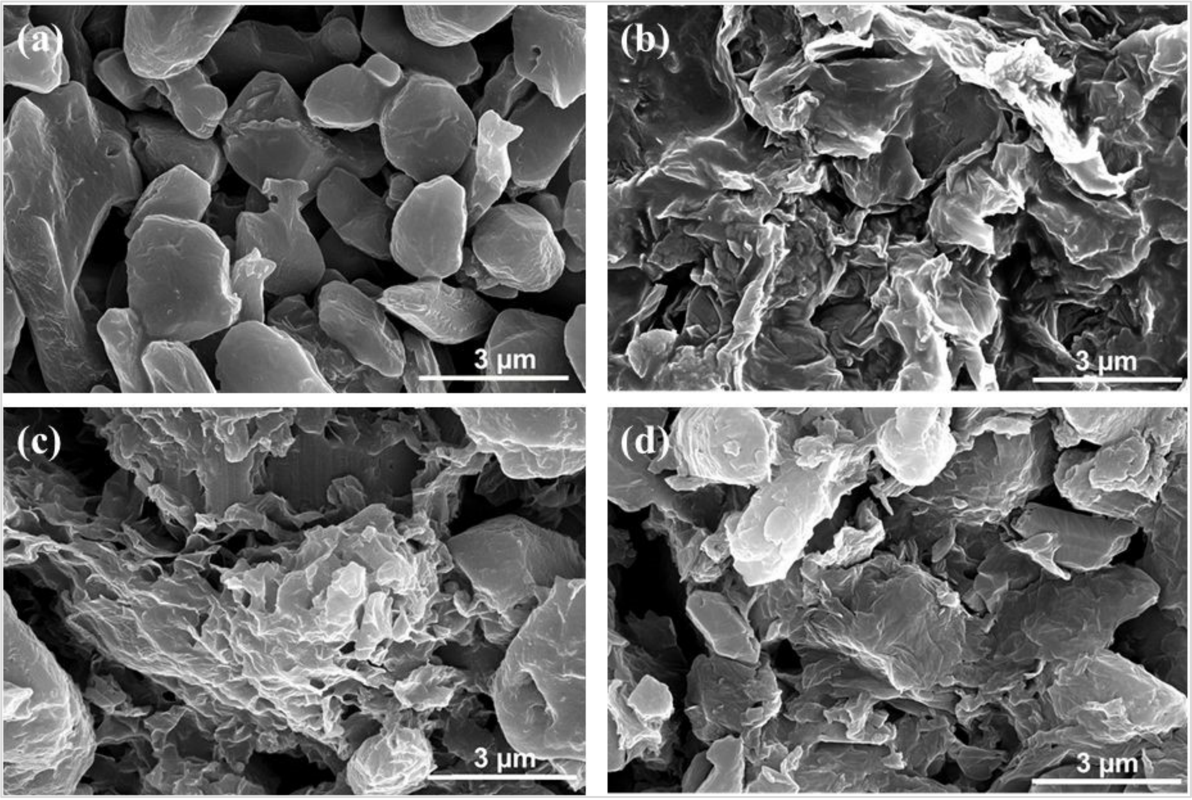

Fig. 2. The FESEM images of (a) Co-MOF; (b) GO; (c) Co-MOF-GO5; (d) Co-MOF-GO10.

Morphological analysis by FESEM reveals clear modifications that directly correlate with supercapacitor performance. Pristine Co-MOF shows well-defined polyhedral particles containing smooth surfaces, while the GO displays an archetypal, layered, and wrinkled nanosheet morphology (Fig. 2a and 2b**)**. In the Co-MOF-GO5 composite, the Co-MOF particles are homogeneously distributed and firmly attached to the GO sheets, forming a uniform, porous structure (Fig. 2c). The well-integrated homogeneous morphology can provide plentiful electrochemically active sites, narrow ion diffusion pathways, and efficient electron transport, leading to enhanced capacitive performance. On the other hand, Co-MOF-GO10 exhibits a denser morphology, with fractional restacking of GO sheets and accumulation of Co-MOF particles, resulting from the higher GO content (Fig. 2d), which may block active sites and hinder electrolyte diffusion. The thermal stability of the synthesized Co-MOF, GO, and their composites was studied using fine-powder samples in the temperature range from 30 to

View Article Online
DOI: 10.1039/D6MA00515B

800 °C under a N_2 atmosphere, as shown in Fig. S2 in the ESI. Initial ~28% weight loss at ~120 °C may be attributed to the exclusion of all four coordinated water molecules, and the second round of weight loss (~35%) near 400-450 °C can be attributed to degradation of the organic ligand.

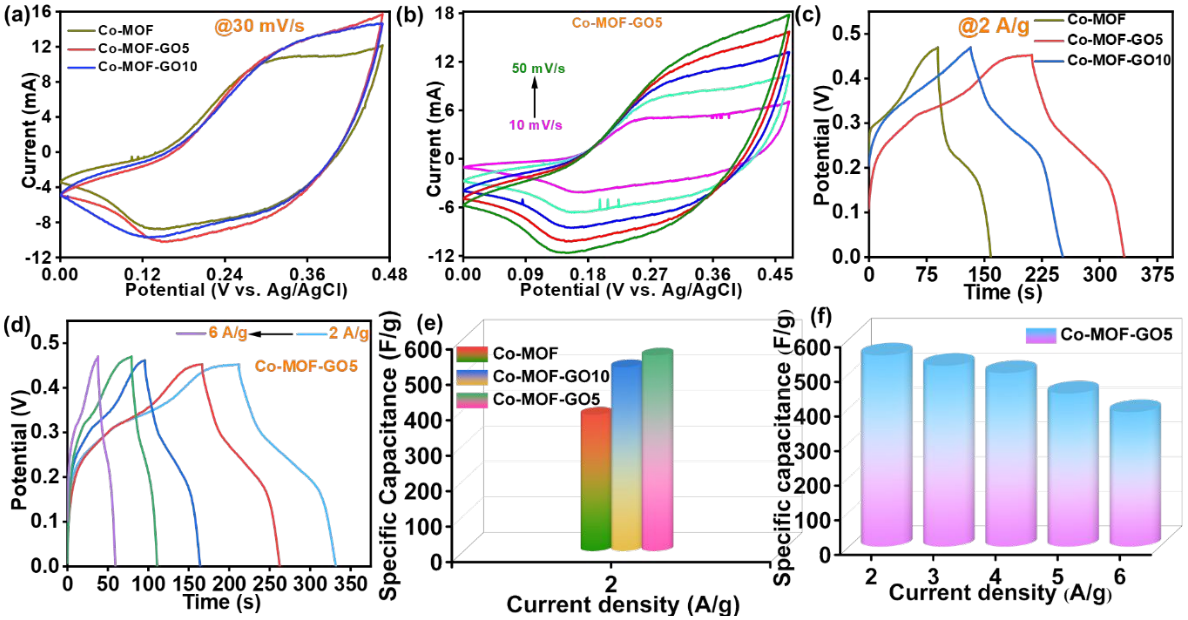

Fig. 3. (a) Comparison of CV curves for Co-MOF, Co-MOF-GO5, and Co-MOF-GO10 at scan rates of 30 mV/s in a three-electrode system; (b) CV curves of Co-MOF-GO5 at different scan rates from 10 mV/s to 50 mV/s; (c) Comparison of GCD plots of Co-MOF, Co-MOF-GO5, and Co-MOF-GO10 at 2 Ag^{-1}. (d) GCD plots of Co-MOF-GO5 at different current densities from 2 A g^{-1} to 6 A g^{-1}. (e) Relative specific capacitance for all the materials at 2 A g^{-1}. (f) Corresponding specific capacitances for Co-MOF-GO5 at different current densities.

The prime assessment of the electrochemical properties of Co-MOF and their GO composites was conducted in a three-electrode system, where a Ni-foam current collector loaded with the MOF or MOF-GO composite-based materials was used as the working electrode (WE), Ag/AgCl in saturated KCl was used as the reference electrode (RE), a Pt-wire acted as the counter electrode (CE), and 1 M KOH was used as the electrolyte.[51-55] The applied potential window of the working electrode was assessed by anodically cyclic scanning from 0 to 0.47 V (vs. Ag/AgCl), providing the reversible redox peaks of Co^{2+}/Co^{3+} in Co-MOF and its composites. The cyclic voltammetry (CV) of the pristine Ni-foam electrode shows that Ni-foam exhibits minute redox activity, and the area under the curve of bare Ni-foam CV is much smaller than that of the Co-MOF or MOF composite-loaded electrodes (Fig. S3 in the ESI). Previous study revealed a very less specific capacitance of bare Ni-foam, with a specific

View Article Online
DOI: 10.1039/D6MA00515B

capacitance of 1.31 F g^{-1} [20,37] Co-MOF-GO composites modified electrode exhibits a higher enclosed area in the CV plot than that of the Co-MOF, as evidenced from Fig. 3a. Fig. 3b displays the individual voltammogram of the Co-MOF-GO5 modified electrode at different scan rates, showing the reversible redox behaviour of the electrode material with oxidation and reduction peaks at 0.257 V and 0.17 V, respectively, at a scan rate of 10 mV/s, conforming to the Co^{2+}/Co^{3+} redox cycle. The steady increase in current with increasing scan rate indicates the highly reversible nature of the electrode material. The specific capacitance values for the Co-MOF, Co-MOF-GO5, and Co-MOF-GO10 electrodes are determined based on their GCD curves and compared in Fig. 3c. The Co-MOF-GO5 composite's GCD curves at diverse current densities are shown in Fig. 3d. The nature of the CV and GCD clearly indicates the prominent pseudocapacitance behavior of the material, however, mixed with the surface double-layer capacitance also. The detailed CV and GCD studies of the Co-MOF are shown in Fig. S4 in the ESI. Co-MOF-GO5 displays higher capacitance than the parent Co-MOF and Co-MOF-GO10 at a current density of 2 A g^{-1}. Remarkably, the value of specific capacitance for the Co-MOF and Co-MOF-GO10 is measured as 385 F g^{-1} and 519 F $g^{-1,}$ whereas the same is determined as 552 F g^{-1} for the Co-MOF-GO5 (Fig. 3e). Fig. 3f indicates the good rate competence with capacitance retention as the current density increases from 2 to 6 A g^{-1}.

According to Dunn's method, the contributions of surface-limited EDLC and diffusion-limited pseudocapacitive behavior to the total storage performance were estimated from CV curves studied at different scan rates.[20,37,51,56] The electrochemical mechanism can be examined using the following equations:

$$\boldsymbol{i = av^b} \ \ldots\ldots\ldots\ldots\ldots \ (6)$$

$$\boldsymbol{log(i) = loga + blog(v)} \ldots\ldots\ldots \ (7)$$

Where the peak current is denoted by *i*, v represents the scan rate, and a and b are adjustable parameters. If b = 1, *i* will be linearly correlated with the scan rate, and the overall electrochemical mechanism is controlled by the non-faradic process on the electrode surface, implying the electrode materials' EDLC behavior. On the other hand, if *i* is proportional to the square root of the scan rate (b = 0.5), the diffusion of ions controls the electrochemical process, and storage behavior depends on the faradic pseudocapacitive nature. The capacitive and diffusive involvement of energy storage can be quantitatively resolved using the following equation proposed by Dunn et al., comprising the current response and scan rate:

$$\boldsymbol{i = k_1 v + k_2 v^{1/2}} \ \ldots\ldots\ldots\ldots\ldots\ldots\ldots \ (8)$$

View Article Online
DOI: 10.1039/D6MA00515B

$$\frac{k_1 v}{i} + \frac{k_2 v^{\frac{1}{2}}}{i} = 1 \ldots\ldots\ldots\ldots\ldots\ldots \text{(9)}$$

Where k_1 and k_2 are coefficients and can be calculated from $i/v^{1/2}$ vs the square root of the scan rate plot. In this equation, $k_1 v/i$ infers the capacitive involvement, while $k_2 v^{1/2}/i$ denotes the diffusion-controlled influence.

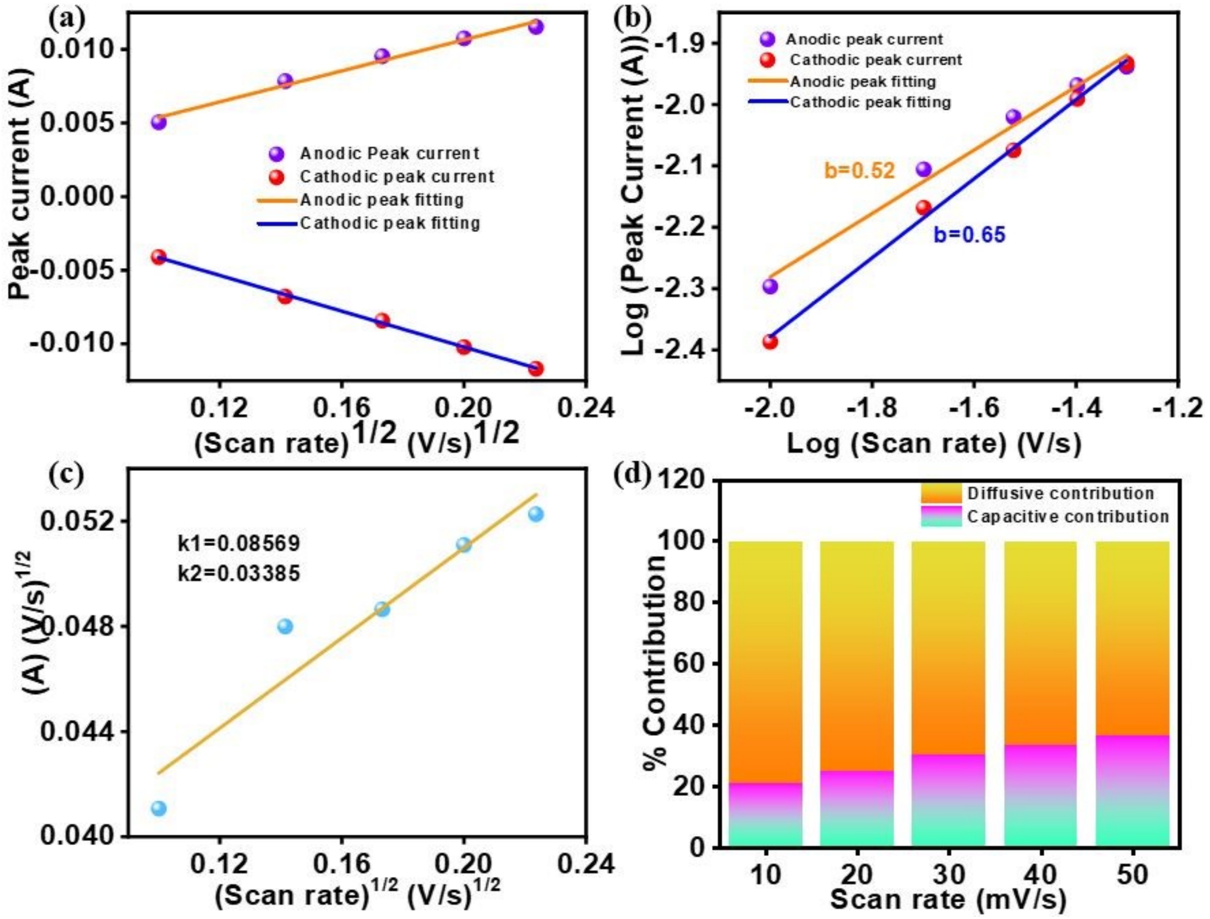

Fig. 4. Mechanistic insights into charge storage for Co-MOF-GO5. (a) Peak current vs. the square root of the scan rate plot; (b) Calculation of b values from the anodic and cathodic peak-fitting plot; (c) Determination of k_1 and k_2 values from the $i/v^{1/2}$ plot; (d) Diffusive-capacitive contribution plot.

In the scan-rate-dependent CV studies, the peak current of the Co-MOF-GO5 electrode is linearly correlated with the square root of the scan rate (Fig. 4a), indicating a major extent of pseudocapacitive behavior. The Dunn's method was employed for the estimation of the contributions of the surface-limited EDLC and the diffusion-limited pseudocapacitive progressions to the total storage behaviour from CV curves.[20, 37] The logarithm plot for the anodic or cathodic peak currents vs. the logarithm of scan rate in Fig. 4b evaluates the primary diffusive nature of the system, as the b value is determined to be ~0.65 from cathodic peak

View Article Online
DOI: 10.1039/D6MA00515B

fitting. The k_1 and k_2 values are determined from Fig. 4c, and the EDLC (capacitive) and pseudocapacitive or diffusive contributions are subsequently calculated using Equation 8. The discrete contributions of capacitive and diffusion-controlled pseudocapacitive behaviours at different scan rates are shown in Fig. 4d. From the figures, it is projected that a diffusion-controlled pseudocapacitive mechanism prevails in the energy storage mechanism of Co-MOF-GO5.

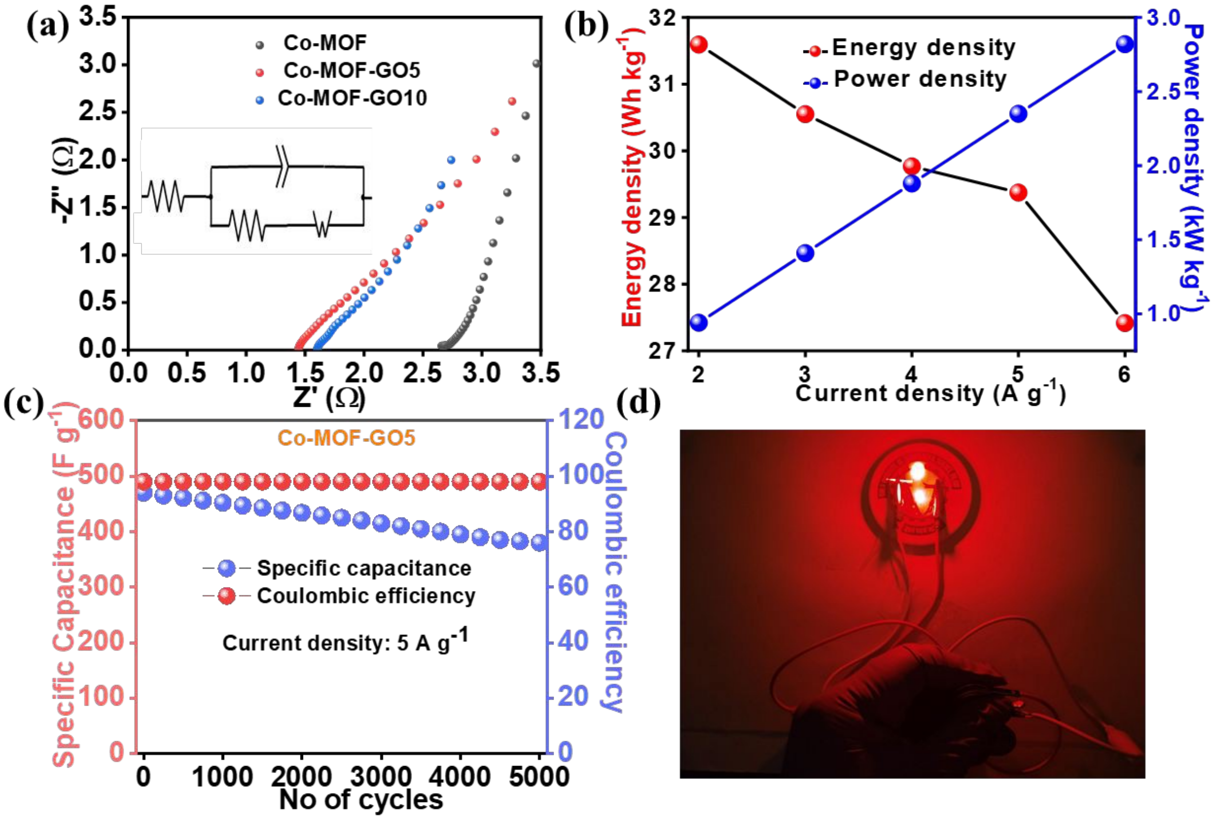

Fig. 5. (a) EIS study of Co-MOF, Co-MOF-GO5, Co-MOF-GO10 electrodes (The equivalent circuit is given in the inset); (b) Plots of the energy and power density as a function of the current density; (c) Charge-discharge cycle performance of the Co-MOF-GO5-based supercapacitor for 5000 cycles at a current density of 5 A g^{-1}; (d) Lighting of a light-emitting diode by the two CR2032 coin-cell devices connected in series.

The transport properties of the Co-MOF, Co-MOF-GO5, and Co-MOF-GO10 electrodes were inspected using electrochemical impedance spectroscopy (EIS). The Nyquist plots for the Co-MOF and the composite modified electrode were obtained over a frequency range from 1 Hz to 10 kHz (Fig. 5a). In the high-frequency region, the plots display the semicircles which provide the charge transfer resistances (R_{CT}) of 2.33 Ω, 1.2 Ω, and 1.8 Ω for Co-MOF, Co-MOF-GO5, and Co-MOF-GO10, respectively, after fitting in an equivalent

View Article Online
DOI: 10.1039/D6MA00515B

circuit given in inset. The result indicates the lowest resistance during ion transport in Co-MOF-GO5. Furthermore, Co-MOF, Co-MOF-GO5, and Co-MOF-GO10 composites exhibit different solution resistances (R_S) of 2.64 Ω, 1.4 Ω, and 1.62 Ω, respectively, indicating that Co-MOF-GO5 exhibits the highest relations among the electrolyte and the electrode materials. At lower frequencies, plots show a straight line, indicating the presence of Warburg impedance. The Warburg impedance phase angle of ~45° in Co-MOF-GO5 reflects better charge transfer and improved ion diffusion, likely due to the well-matched Co-MOF and GO combination. This synergy improves the electrochemical kinetics and contributes to the superior supercapacitor performance of Co-MOF-GO5.

In a three-electrode configuration, the Co-MOF-GO5 displays a decent energy density of 33 Wh kg^{-1} at a power density of 2.9 kW kg^{-1}, as shown in Fig. 5b. This validates the Co-MOF-GO5 electrode's ability to sustain high power and energy densities simultaneously. Yet again, the Co-MOF-GO5-based supercapacitor delivers higher performance than bare Co-MOF and Co-MOF-GO10, maintaining around 80% capacitive retention and achieving 98% coulombic efficiency even after 5000 successive charge-discharge cycles, indicating durable supercapacitive performance (Fig. 5c).[48] For validating the state-of-the-art device, we engineered CR2032 coin cells to show practical, real-world applications. We assembled a symmetric coin cell using Co-MOF-GO5 with equal mass loading in both electrodes. When two fabricated coin cells are connected in series, they can effectively power a light-emitting diode (LED, ~1.8 V) bulb for a few minutes (Fig. 5d). These insights highlight the high potential of Co-MOF-GO5 as a promising material for developing effective energy storage devices for real-world energy applications.

View Article Online
DOI: 10.1039/D6MA00515B

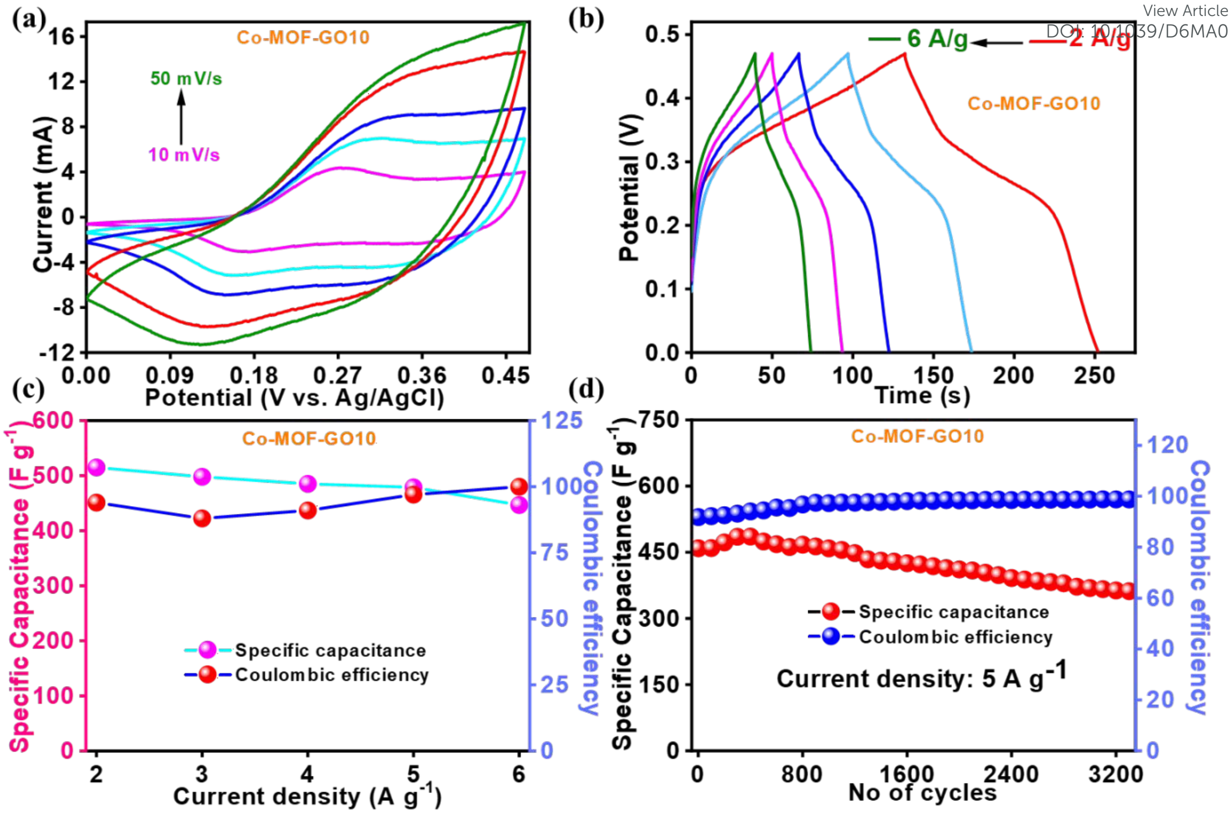

Fig. 6. Supercapacitor performance of Co-MOF-GO10. (a) CV curves of Co-MOF-GO10 at different scan rates from 10 mV/s to 50 mV/s; (b) GCD plots of Co-MOF-GO10 at different current densities from 2 A g^{-1} to 6 A g^{-1}; (c) Corresponding specific capacitances and coulombic efficiency of Co-MOF-GO10 electrode at different current densities; (d) Charge-discharge cycle performance of the Co-MOF-GO10-based supercapacitor for 3300 cycles at a current density of 5 A g^{-1}.

Fig. 6a shows the individual voltammogram of the Co-MOF-GO10 modified electrode at different scan rates, showing the reversible redox behaviour of the electrode material with oxidation and reduction peaks at 0.259 V and 0.172 V, respectively, at a scan rate of 10 mV/s owing to Co^{2+}/Co^{3+} redox transition when measured in a three-electrode system. The Co-MOF-GO10 composite's GCD curves at diverse current densities are shown in Fig. 6b. The specific capacitance for the Co-MOF-GO10 is measured as 519 F g^{-1} at 2 A g^{-1} current density. Co-MOF-GO10 also reveals a high-rate capability as it shows only a slight decrease in specific capacitance with increasing current densities (Fig. 6c). The Co-MOF-GO10-based supercapacitor exhibits higher cyclic durability than bare Co-MOF but lesser than Co-MOF-GO5 as it maintains around 77% capacitive retention and shows 98% coulombic efficiency after 3300 successive charge-discharge cycles (Fig. 6d). We have also calculated the b-values and percentage contribution for Co-MOF and Co-MOF-GO10, and compared them with Co-

View Article Online
DOI: 10.1039/D6MA00515B

MOF-GO5. It was observed that the bare Co-MOF has the maximum diffusion mechanism, and Co-MOF-GO10 has the maximum surface EDLC contribution; whereas Co-MOF-GO5 has a balanced contribution of EDLC (capacitive) and pseudocapacitive or diffusive contributions between both of them (Fig. 3b, Fig. 6a, Fig. S4a, and Fig. S5). To support the performance of Co-MOF-GO5 compared to pristine Co-MOF and 10% composite, the electrochemically active surface area (ECSA) was measured in the non-Faradaic region in the cyclic voltammetry. Co-MOF-GO5 demonstrates an ECSA of 281 cm^2, higher than the pure Co-MOF value of 96 cm^2, and Co-MOF-GO10 is 106 cm^2 (Fig. S6, ESI). Pristine Co-MOF exhibits the lowest ECSA due to aggregation, thereby effectively reducing the electrochemically accessible active sites. The Co-MOF-GO5 achieves the highest ECSA because it contains a moderate amount of GO, which provides an ideal 2D template that prevents Co-MOF aggregation, yielding highly dispersed particles with fully exposed MOF active sites and improved charge transfer. On the other hand, a higher GO loading in the Co-MOF-GO10 sample results in excess GO sheets wrapping around the MOF particles, physically blocking their accessible active sites and reducing the ECSA. Despite the lower ECSA, Co-MOF-GO10 exhibits the highest EDLC due to its higher GO content, demonstrating a storage mechanism based on an electrostatic double-layer arrangement. The synergistic effect of a moderate amount of GO and Co-MOF in Co-MOF-GO5 results in higher ECSA and comparatively better CV-enclosed area and specific capacitance than in Co-MOF-GO10. Overall, Co-MOF-GO5 shows a better or comparable energy storage performance compared to the recently reported MOFs or MOF-graphene composites, as shown in Table S1 in ESI. The synergy of optimal GO incorporation in Co-MOF-GO5 via the *in-situ* synthesis process provides better interfacial coupling, faster charge transfer, and the highest ECSA, thereby ameliorating the energy storage properties of Co-MOF-GO5 compared to pristine Co-MOF and Co-MOF-GO10.

4. Conclusion:

A scalable *in-situ* approach was employed with a non-aromatic simple aliphatic succinate-based dicarboxylate linker, inexpensive and commercially accessible precursors, and a water-mediated synthesis route, which results in lower synthetic complexity, better scalability, lower cost, and a greener synthesis pathway to integrate GO into a cobalt succinate-based CO-MOF, forming an efficient hybrid electrode for high-performance supercapacitor energy storage applications by combining diffusion-controlled pseudocapacitance from Co-redox centres, the surface EDLC contribution from GO. The adjusted Co-MOF-GO5 composite delivers a high

View Article Online
DOI: 10.1039/D6MA00515B

specific capacitance of 552 F g^{-1}at 2 A g^{-1}, driven by the synergistic interplay between Co^{2+}/Co^{3+} redox activity, GO-enabled charge transport, and the highest ECSA (281 cm^2). Electrochemical impedance analysis reveals reduced charge-transfer resistance and accelerated ion diffusion in Co-MOF-GO5 compared to pristine Co-MOF and higher GO-loaded composites. The electrode delivers an energy density of 33 Wh kg^{-1} at a power density of 2.9 kW kg^{-1}, with excellent lateral durability during charging-discharging cycles (~80% retention over 5000 cycles), stabilized through a cooperative heterointerface mechanism. A symmetric CR2032 device based on Co-MOF-GO5 successfully powers a commercial LED, authenticating its practical viability. The findings demonstrate the importance and utility of precisely *in situ*-forming MOF/GO composites to overcome the significant conductivity limitations of MOFs and provide a viable design pathway for high-performance, cost-effective supercapacitor electrodes.

Conflicts of interest

There are no conflicts to declare.

Electronic Supplementary Information

Electronic Supplementary Information (ESI) available: TGA for Co-MOF and Co-MOF-GO composites; supporting CV and GCD studies of Co-MOF for supercapacitor parameters.

Acknowledgments

C. C. acknowledges the Department of Science and Technology, Govt. of India, for providing instrumental facilities through the PURSE Project No. SR/PURSE/2020/20 (G) at BITS Pilani Hyderabad Campus. S. K. is thankful to BITS Pilani Hyderabad Campus for the institutional fellowship and for the instrumental facilities.

References:

1. B. Dunn, H. Kamath and J. M. Tarascon, *Science*, 2011, **334**, 928-935.
2. M. C. Das, S. C. Pal and B. Chen, *Joule*, 2022, **6**, 22-27.
3. N. S. Lewis, *MRS Bull.*, 2007, **32**, 808-820.
4. E. Kabalci, *Energy Convers. Manage.*, 2013, **72**, 51-59.
5. M. Talaat, M. A. Farahat and M. H. Elkholy, *Energy*, 2019, **170**, 668-678.
6. M. Winter and R. J. Brodd, *Chem. Rev.*, 2004, **104**, 4245-4269.

View Article Online
DOI: 10.1039/D6MA00515B

7. Y. Dong, J. Liu, H. Zhang, Q. Li, F. Mao, A. Lu, H. Wu, K. Wang, C. Zhang and Q. Zhang, *SmartMat*, 2023, **4**, 1159.

8. X. Yang, Y. Tian, S. Li, Y.-P. Wu, Q. Zhang, D.-S. Li and S. Zhang, *J. Mater. Chem. A*, 2022, **10**, 12225-12234.

9. S. Xu, J. Wu, X. Wang and Q. Zhang, *Chem. Sci.*, 2023, **14**, 13601-13628.

10. K. Wang, Z. Wang, J. Liu, C. Li, F. Mao, H. Wu and Q. Zhang, *ACS Appl. Mater. Interfaces*, 2020, **12**, 47482-47489.

11. C. Choi, D. S. Ashby, D. M. Butts, R. H. DeBlock, Q. Wei, J. Lau and B. Dunn, *Nat. Rev. Mater.*, 2020, **5**, 5-19.

12. Y. Liang and Y. Yao, *Nat. Rev. Mater.*, 2023, **8**, 109-122.

13. K. Padmasri, S. Khan, S. A. Singh, C. Chakraborty and P. Doddipatla, *ACS Omega*, 2026, **11**, 23480-23489.

14. Y. Ma, X. Xie, W. Yang, Z. Yu, X. Sun, Y. Zhang, X. Yang, H. Kimura, C. Hou, Z. Guo and W. Du, *Adv. Compos. Hybrid Mater.*, 2021, **4**, 906-925.

15. P. Naskar, A. Maiti, P. Chakraborty, D. Kundu, B. Biswas and A. Banerjee, *J. Mater. Chem. A*, 2021, **9**, 1970-2017.

16. L. L. Zhang and X. S. Zhao, *Chem. Soc. Rev.*, 2009, **38**, 2520–2531.

17. T. Wang, X. Zang, X. Wang, X. Gu, Q. Shao and N. Cao, *Energy Storage Mater.*, 2020, **30**, 367-384.

18. A. M. Bryan, L. M. Santino, Y. Lu, S. Acharya and J. M. D’Arcy, *Chem. Mater.*, 2016, **28**, 5989-5998.

19. C. Yuan, H. B. Wu, Y. Xie and X. W. Lou, *Angew. Chem. Int. Ed.*, 2014, **53**, 1488-1504.

20. S. Khan, S. Chand, P. Sivasakthi, P. K. Samanta and C. Chakraborty, *Small*, 2024, **20**, 2401102.

21. S. Khan, S. Chand, P. Thippeswamy, D. Ghosh and C. Chakraborty, *Sustainable Energy Fuels*, 2025, **9**, 2698-2706.

22. H. C. Zhou, J. R. Long and O. M. Yaghi, *Chem. Rev.*, 2012, **112**, 673-674.

23. H. C. Zhou and S. Kitagawa, *Chem. Soc. Rev.*, 2014, **43**, 5415-5418.

24. G. Chakraborty, I. H. Park, R. Medishetty and J. J. Vittal, *Chem. Rev.*, 2021, **121**, 3751-3891.

25. J. Liu, X. Song, T. Zhang, S. Liu, H. Wen and L. Chen, *Angew. Chem. Int. Ed.*, 2021, **60**, 5672-5687.

26. X. Xiao, S. Tao, H. Lian, Y. Tian, W. Deng, H. Hou, G. Zou and X. Ji, *ACS Nano*, 2024, **18**, 28444-28455.

View Article Online
DOI: 10.1039/D6MA00515B

27. D. Feng, T. Lei, M. R. Lukatskaya, J. Park, Z. Huang, M. Lee, L. Shaw, S. Chen, A. A. Yakovenko, A. Kulkarni and J. Xiao, *Nat. Energy*, 2018, **3**, 30-36.

28. M. Zhao, Y. Wang, Q. Ma, Y. Huang, X. Zhang, J. Ping, Z. Zhang, Q. Lu, Y. Yu, H. Xu and Y. Zhao, *Adv. Mater.*, 2015, **27**, 7372-7378.

29. S. Khan, A. Biswas, S. Chand, C. Chakraborty, *Chem. Commun.*, 2026, **62**, 9477-9480.

30. S. Halder, A. K. Pradhan, S. Khan, and C. Chakraborty, *Energy Adv.*, 2023, **2**, 1713-1723.

31. A. Husain, N. Hussain and S. M. Mobin, *J. Mater. Chem. A*, 2026, **14**, 8351-8360.

32. K. Chen, X. L. Wang, W. Hu, Q. Kong, H. Pang and Q. Xu, *Small Struct.*, 2022, **3**, 2100200.

33. Z. Xia, X. Jia, X. Ge, C. Ren, Q. Yang, J. Hu, Z. Chen, J. Han, G. Xie, S. Chen and S. Gao, *Angew. Chem.*, 2021, **133**, 10316-10327.

34. F. L. Li, P. Wang, X. Huang, D. J. Young, H. F. Wang, P. Braunstein and J. P. Lang, *Angew. Chem. Int. Ed.*, 2019, **58**, 7125-7129.

35. F. B. Ajdari, E. Kowsari, M. N. Shahrak, A. Ehsani, Z. Kiaei, H. Torkzaban, M. Ershadi, S. K. Eshkalak, V. Haddadi-Asl, A. Chinnappan and S. Ramakrishna, *Coord. Chem. Rev.*, 2020, **422**, 213441.

36. S. J. Shin, J. W. Gittins, C. J. Balhatchet, A. Walsh and A. C. Forse, *Adv. Funct. Mater.*, 2024, **34**, 2308497.

37. S. Khan, S. Chand and C. Chakraborty, *Chem. Eng. J.*, 2025, **516**, 164232.

38. Q. Liu, Z. Guo, C. Wang, S. Guo, Z. Xu, C. Hu, Y. Liu, Y. Wang, J. He and W. Y. Wong, *Adv. Sci.*, 2023, **10**, 2207545.

39. R. Sahoo, S. Ghosh, S. Chand, S. C. Pal, T. Kuila and M. C. Das, *Compos. Part B Eng.*, 2022, **245**, 110174.

40. Z. Xia *et al.*, *Angew. Chem.*, 2021, **133**, 10316-10327.

41. S. Ramesh, S. Khandelwal, K. Y. Rhee and D. Hui, *Compos. Part B Eng.*, 2018, **138**, 45-54.

42. P. Srimuk, S. Luanwuthi, A. Krittayavathananon and M. Sawangphruk, *Electrochim. Acta*, 2015, **157**, 69-77.

43. S. Gautam, S. Rialach, S. Paul and N. Goyal, *RSC Adv.*, 2024, **14**, 14311-14339.

44. V. Jabbari, J. M. Veleta, M. Zarei-Chaleshtori, J. Gardea-Torresdey and D. Villagrán, *Chem. Eng. J.*, 2016, **304**, 774-783.

45. C. C. Hou, L. Zou, Y. Wang and Q. Xu, *Angew. Chem. Int. Ed.*, 2020, **59**, 21360-21366.

46. P. Zhang, B. Y. Guan, L. Yu and X. W. Lou, *Angew. Chem.*, 2017, **129**, 7247-7251.

47. M. Du, D. Song, A. Huang, R. Chen, D. Jin, K. Rui, C. Zhang, J. Zhu and W. Huang, *Angew. Chem.*, 2019, **131**, 5361-5366.

48. S. Khan, S. Halder, S. Chand, A. K. Pradhan and C. Chakraborty, *Dalton Trans.*, 2023, **52**, 14663-14675.

49. C. Livage, C. Egger and G. Férey, *Chem. Mater.*, 2001, **13**, 410-414.

50. S. Khan, A. K. Shukla, A. Bhattacharya, S. Chand and C. Chakraborty, *Inorg. Chem.*, 2024, **63**, 18438-18447.

51. T. M. Gür, *Energy Environ. Sci.*, 2018, **11**, 2696-2767.

52. Z. Xia *et al.*, *Angew. Chem.*, 2021, **133**, 10316-10327.

53. R. Abazari, S. Sanati, A. Morsali, A. Slawin and C. L. Carpenter-Warren, *ACS Appl. Mater. Interfaces*, 2019, **11**, 14759-14769.

54. F. Cao, M. Zhao, Y. Yu, B. Chen, Y. Huang, J. Yang, X. Cao, Q. Lu, X. Zhang, Z. Zhang and C. Tan, *J. Am. Chem. Soc.*, 2016, **138**, 6924-6927.

55. R. Abazari *et al.*, *ACS Appl. Mater. Interfaces*, 2019, **11**, 14759-14769.

56. S. Pervez and M. Z. Iqbal, *Small*, 2023, **19**, 2305059.

View Article Online
DOI: 10.1039/D6MA00515B

Data availability statement (DAS)

The data supporting this article have been included in the article or as part of the Supplementary Information.

Sincerely yours,

Dr. Chanchal Chakraborty
Assistant Professor
BITS Pilani, Hyderabad Campus
Hyderabad, India